

A Proof-of-Concept Membrane Module Concept for Solar Thermal Water Splitting Using Oxygen Transport Membranes

Christopher Hall, Falk Schulze-Küppers,* Kai Bittner, Bernd Büddefeld, Nikolaos Margaritis, Jörg Wolters, Sonja Groß-Barsnick, Juan Pablo Rincon Duarte, Nicole Carina Neumann, and Ghaleb Natour

Solar thermal water splitting using oxygen transport membranes enables sustainable hydrogen production and can thus play a key role in the emerging hydrogen economy. Membrane reactors potentially reduce temperature required by shifting the concentration equilibrium, thereby increasing the efficiency of thermal water splitting. This work presents a scaled-up proof-of-concept (PoC) module design for solar thermal water splitting applications utilizing oxygen transport membranes in relevant environments. The PoC module is based on a flexible and scalable stack design with parallel-oriented, membrane-containing layers, which supports the scalability of the concept. Solar heat integration is optimized for direct irradiation by a High Flux Solar Simulator. Key outcomes include focal point adjustments and design modifications using an irradiated copper plate to mitigate hot spots. The PoC module's material concept prevents thermal stresses and ensures gas-tight sealing of the membranes at an operating temperature of 850 °C under reducing and corrosive atmospheres. Optimal flow rates for steam (30–213 mmol min⁻¹) and methane (8–54 mmol min⁻¹) are calculated for the PoC module, resulting in efficient hydrogen (7–51 mmol min⁻¹) and syngas (22–156 mmol min⁻¹) production, using a membrane area of 167 cm², with H₂O and CH₄ conversion rates of 25% and 95%, respectively.

hydrogen spans several industrial sectors including transportation.^[1,2] Projections indicate an escalating role for hydrogen in steel manufacturing^[3,4] and chemical production^[5] in the future. Hydrogen is a clean alternative to fossil fuels with the potential to decarbonize sectors that are difficult to reduce. It is a clean alternative to fossil fuels because its use as an energy source produces only water as a by-product, eliminating direct greenhouse gas emissions. The generation of hydrogen, particularly the environmentally sustainable form of solar-thermal hydrogen, holds promise as a viable route for the direct production of renewable fuels or green hydrogen.^[6]

The production of green hydrogen based on the process of water splitting, driven by solar energy, takes place at temperatures above 2500 Kelvin.^[7] Technologies that can safely operate at lower temperatures are currently under investigation. Besides high-temperature water electrolysis and solar biomass gasification,^[8] thermochemical

water splitting^[9] is one of the most promising technologies^[8,10–12] with high theoretical efficiency potential.^[13,14] Thermochemical water splitting can be performed via a two-step redox cycle using metal oxides. In the first step, the metal oxide undergoes thermal reduction, releasing oxygen at ≈1500 °C. In the second step, the reduced metal oxide reacts with steam at around 1000 °C,

1. Introduction


Hydrogen has emerged as a pivotal solution for mitigating carbon emissions and accomplishing sustainable energy objectives, including climate neutrality, ensuring energy security, and the integration of renewable energy sources. The current use of

C. Hall, F. Schulze-Küppers, K. Bittner, B. Büddefeld, N. Margaritis, J. Wolters, S. Groß-Barsnick, G. Natour
Forschungszentrum Jülich GmbH
Institute of Technology and Engineering (ITE)
Leo-Brandt-Str. 1, D-52425 Jülich, Germany
E-mail: f.schulze@fz-juelich.de

K. Bittner
Faculty of Mechanical Engineering
RWTH Aachen University
52062 Aachen, Germany

J. P. R. Duarte, N. C. Neumann
Deutsches Zentrum für Luft- und Raumfahrt e.V.
Institut of Future Fuels, Linder Höhe
51147 Köln, Germany

G. Natour
ISF, Faculty of Mechanical Engineering
RWTH Aachen University
52062 Aachen, Germany

 The ORCID identification number(s) for the author(s) of this article can be found under <https://doi.org/10.1002/ente.202402191>.

© 2025 The Author(s). Energy Technology published by Wiley-VCH GmbH. This is an open access article under the terms of the Creative Commons Attribution License, which permits use, distribution and reproduction in any medium, provided the original work is properly cited.

DOI: 10.1002/ente.202402191

reabsorbing oxygen while producing hydrogen in its gaseous form.^[11,15] Combining the two-stage thermochemical water-splitting process with co-production of electricity with excess heat, hydrogen could be produced at a price of around \$4.55/kg, with the potential to meet the U.S. DOE cost target of \$2/kg.^[12] To optimize the process and minimize expenses, the oxidation and reduction of metal oxides can be executed in a single-step process using a mixed ion-electron conducting membrane (MIEC). The transport of oxygen through the MIEC membrane, is the result of the joint diffusion of oxygen anions and electrons through the membrane under the driving force of a gradient in chemical potential of oxygen which can be related to the oxygen partial pressures on the feed and sweep side (**Figure 1**). Laboratory-scale experiments have demonstrated that the temperature for ceramic membrane-assisted steam thermolysis can be reduced to below 1000 °C.^[16]

The coupling of water splitting and an oxidation process is composed of three steps. The initial step, the water splitting reaction, occurs on the membrane surface on the feed side (steam line) at high temperature. During this process, steam is split into hydrogen H₂ and oxygen. The oxygen adsorbs on the membrane surface and is incorporated into the lattice. Through a process of condensation, unreacted water is efficiently removed at the retentate outlet, resulting in the production of high-purity hydrogen. The MIEC membrane's oxygen conductivity enables the selective removal of oxygen, thereby facilitating water splitting and enhancing the hydrogen production rate. The second step is the process of oxygen diffusion through the membrane. Assuming that oxygen vacancies are the mobile ionic defects, the interaction of oxygen with the membrane can be represented by a chemical reaction of the form



To incorporate uncharged oxygen O₂ into a regular oxygen site in the crystal lattice O_O[×], half an oxygen molecule from the gas phase, a double positively charged oxygen vacancy in the crystal lattice V_O^{••} and two free, negatively charged electrons e⁻ are required. To maintain electroneutrality, single positively charged electron holes and free, single negatively charged electrons are in equilibrium. The driving force of oxygen permeation is generally

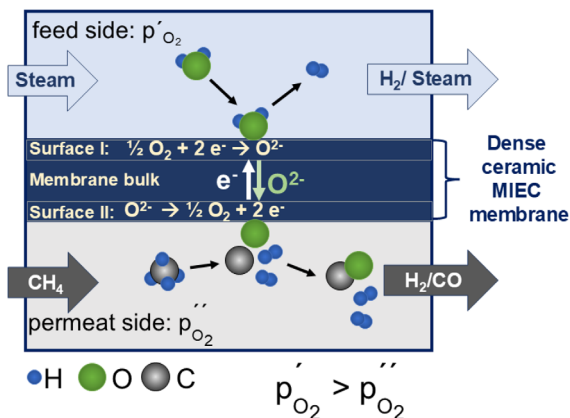


Figure 1. Scheme of coupling water splitting and an oxidation process inside the oxygen transport membrane module, adapted from.^[24]

assumed to be the oxygen partial pressure gradient across the membrane according to the Wagner equation:

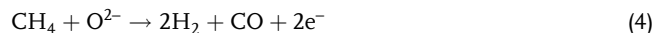
$$j_{\text{O}_2} = -\frac{RT}{4F^2L} \int_{\ln p'_{\text{O}_2}}^{\ln p''_{\text{O}_2}} \sigma_{\text{amb}} d \ln p_{\text{O}_2} \quad (2)$$

where j_{O_2} is the oxygen permeation, R is the gas constant, T is the Temperature, F is the Faraday constant, L is the membrane thickness, p'_{O_2} and p''_{O_2} the oxygen partial pressures at the high-pressure side and low-pressure side, and σ_{amb} the ambipolar conductivity with.

$$\sigma_{\text{amb}} = \frac{\sigma_{\text{el}} \cdot \sigma_{\text{ion}}}{\sigma_{\text{el}} + \sigma_{\text{ion}}} \quad (3)$$

where σ_{el} and σ_{ion} the electron and the ionic conductivity is.^[17]

The third step is the oxidation process at the permeate side (methane line) using a reducing gas (e.g., methane). During this process, oxygen ions are extracted from the lattice and reacts with methane, (CH₄), forming syngas, which consists of hydrogen (H₂) and carbon monoxide (CO).



Oxygen ions may also form and react directly with the reducing sweep gas. Depending on the sweep gas used, additional high-value oxidation products may also be produced, when using, e.g., biomethane or low-value/purity reducing gases (e.g., coke oven gases).^[18,19]

This technology has the advantage of being driven by thermal energy and thus no electrical energy storage units are required. Concentrated solar thermal (CST) plants with a point-focusing system can provide high-temperature heat of up to 1000 °C for this process.^[20–22] Direct sunlight is concentrated by an array of heliostats onto a focal point (FP), where the membrane module could be placed. The coupling of CST with thermal energy storage increases the flexibility of a system by supporting the continuous supply of renewable thermal energy, e.g., in case of reduced solar irradiation in the evening hours or due to clouds. The advantage of this direct integration of renewable thermal energy is on one hand that it eliminates one energy transition step (e.g., from electricity to heat) resulting in sun-to-heat efficiencies of up to 46%^[21] and on the other hand that cost-effective thermal energy storage compared to batteries can be used for an extended operating time.^[23] So far, research has focused on membrane material development for water splitting and testing of a few square centimeters of membrane area^[16,18,24–26] which corresponds to technology readiness level (TRL) 2–3. A good review on water splitting and the performance of MIEC membranes is given in.^[27] However, to evaluate the processes in terms of hydrogen formation rates, the functionality of the technology (TRL 4–5) must be demonstrated.

The integration of the fragile ceramic membranes into a module, and the subsequent integration of the module into CSP, requires further development. Initial research has focused on membrane modules for demonstrating oxygen separation from air,^[28–32] but there is a lack of reports on membrane modules for water splitting at TRL level 4–5. Ensuring homogeneous temperature distribution within the membrane module is a critical challenge, as the temperature-sensitive membrane must not be

exposed to temperature fluctuations. A further challenge that must be addressed is the discrepancy between membrane flux and thermochemical stability. The high-flux membrane materials are not stable under the envisaged conditions,^[33,34] prompting the investigation of iron-substituted SrTiO₃ for low pO₂ and corrosive gas (e.g., H₂O and H₂) applications. The thermochemical stability of this material in syngas derived from the partial oxidation of methane (POM) was demonstrated in the temperature range of 600 to 900 °C for a minimum period of 72 h, during which time the perovskite structure was maintained.^[35] However, research on the long-term stability in these atmospheres is still needed. The developed MIEC membrane material Sr_{0.97}Ti_{0.75}Fe_{0.25}O₃ (STF25) with its specific thermal and chemical volume change and mechanical properties at elevated temperatures^[36–38] determines the requirements of the housing and sealing materials. This is because the functionality of the STF25 membrane material (i.e., oxygen transport) is essential for the process. Therefore, a materials concept for a membrane module is required. This concept should be based on the coefficient of thermal expansion (CTE) and chemical compatibility. This will minimize mechanical stresses within the sealing area between membrane and housing. A final challenge is the lack of experience with the optimal process parameters for the design of such oxygen membrane module. While general trends can be identified from measurements on cm² membrane samples in a laboratory scale, operating parameters specific to a membrane module cannot be determined from these measurements due to differences in experimental setup.

This work moves beyond the existing focus on membrane material development and small-scale testing (TRL 2–3) by developing a functional membrane module approach at TRL 4–5. A systematic methodology was developed to optimize heat integration, process parameters, and material selection, leading to a modular proof-of-concept membrane module. This design facilitates a streamlined, constant-temperature thermochemical water-splitting process using MIEC membranes, representing a significant advance in technological feasibility.

2. Experimental Section

Before designing the membrane module, it is essential to estimate the volume flows of the process gases. The design iteration uses a generalized model, assuming chemical equilibrium and perfect mixing in the gas compartments. Gibbs free energy is minimized in each reaction chamber, which is coupled via the Wagner equation to describe the flow of oxygen ions through the membrane.^[39] The code used for the simulations is published on GitHub.^[40] The equilibrium calculations for the gas compartments were performed using Cantera.^[41]

To obtain the temperature distribution of the proof-of-concept (PoC) module, a stationary thermal model using Ansys Academic Research Workbench 2022 R1 was developed. Heat flux from High Flux Solar Simulator (HFSS) and convective losses inside the cavity were set as boundary conditions. The flux distribution from HFSS was determined using the Finite Element Mesh Ray Tracing (FEMRAY) approach and Solar Power Raytracing Tool (SPRAY).^[42] Convective losses were estimated following

Clausing's procedure for calculating heat losses inside solar receivers.^[43]

For material evaluation, the thermal expansion behavior of ceramic, glass-ceramic, and metallic samples was investigated using dilatometry. Ceramic and glass-ceramic samples were dry-pressed, while metallic samples were cut from sheets. Dilatometric measurements were performed with a Linseis L75V vertical dual rods dilatometer at a heating rate of 3 K min^{−1} up to 910 °C.

Joining tests were carried out by applying a green foil ring of the composite sealant, either glass H with 40 wt% silver (HAg40) or glass H with yttria-stabilized zirconia fibers (H-F), onto a 50 × 50 mm² steel plate and placing the STF25 ceramic membrane with an additional dead load on top. The setup is placed in a chamber furnace and heat treated at 850 °C for 10 h with a heating rate of 2 K min^{−1}.

The PoC module was designed using Catia V5-R62020 software, adhering to the specified boundary conditions, as presented in Table 2.

3. Requirements for the PoC Membrane Module

The boundary conditions for the membrane module design are determined by the process parameters, the membrane material, and geometry to be integrated. In contrast to other designs, discs are used as membranes^[37,44] rather than tubes^[29,30] or plates.^[28,31] Since membrane materials are not yet available on an industrial scale, it is essential that membranes be produced using simple manufacturing technologies that require limited development effort. The membranes are made by tape casting. Information on production can be found here.^[37,44] This has the advantage of testing materials that have not yet been processed on a large scale. The aim is to provide minimum 160 cm² of membrane area in the module. For this purpose, 16-disc shape membranes of STF25 with an open diameter of approx. 48 mm, of which an approx. diameter of 36.5 mm is exposed to the process gases, which are integrated into the module using a glass sealant.^[45] The module development follows the flexible F10 design of the Jülich solid oxide cell (SOC) system, which was created for easy assembly and efficient heat transfer.^[46,47] The SOC stack consists of sheet metal frames that hold the ceramic cell, with four of these membranes able to be integrated per plane. Furthermore, a metal sheets forming a repeating unit, which can be piled up to a stack. Sealing of cells within the steel frame and interconnects can be performed using glass sealant.^[48] This results in 4 membrane planes for the PoC module with a total open membrane area of 167 cm². Each of these must be supplied with steam on the feed side (steam line) and methane on the permeate side (methane line). To obtain these two lines, the membrane must be sealed gas-tight to a membrane window sheet, which carries the membranes. To ensure a compromise between mechanical stability and oxygen flow, the membranes were produced with a thickness of 350 to 400 µm.

From chemical equilibrium calculations using Cantera,^[41] the oxygen partial pressure on the steam line is estimated to be in the order of 10^{−6} bar at module inlet (100% H₂O) and 10^{−17} bar at the outlet, assuming 25% H₂ in the product stream. By assuming stoichiometric (N_{CH4}/N_{O2} = 2) POM, the pO₂ is in the order of

10^{-21} bar at the methane line module outlet. A pressure difference between the two gas compartments and thus mechanical damage to the membranes must be avoided. The module temperature and the required gas flows for H_2O splitting and oxygen separation in the present case can be derived from the process parameters and the material characteristics for the membrane material STF25 given in.^[36] The detailed results of modeling required gas flows using the free Gibbs energy in the individual reaction chambers are presented in Section 3.2. Regarding the use of CH_4 as a sweep gas, the metallic surfaces pose a risk for soot formation when heated to the application temperature. Carbon formation depends on temperature^[49] and usually takes place between 600 and 800 °C. This can cause pipes or cross-sections to clog, which can be reduced and even prevented by adding CO_2 ^[49] or H_2O ^[50] to the methane. For the PoC module to be developed, soot formation is to be solved by means of suitable process control.

The solar thermal power can be supplied by direct irradiation of the PoC module. For this purpose, the cover plate of the module can be irradiated directly by the focused sunlight. However, one challenge is to adapt the heat distribution of the focused solar beam to obtain a homogenous temperature distribution over the PoC module body and control the maximum operating temperature, since the heat flux distribution obtained in the FP of a single-point CST plant has a Gaussian-shape. Therefore, to integrate such solar thermal power into the PoC module with a thermal heat in the range of 800–900 °C, and to avoid large temperature gradients over the PoC module body, the solar flux from the CST system must be homogenized. Various coupling strategies can be used for this purpose. For example, an intermediate heat transfer fluid (e.g., CO_2 , steam) can be used to obtain the heat from the solar receiver and then transfer it to the PoC module with a more homogeneous temperature distribution. This strategy can be very interesting for a scaled-up system, in which a state-of-the-art solar receiver^[51] can be integrated. Other methods to homogenize the heat flux distribution include the application of: 1) flux-guide systems in which solar radiation is more evenly distributed after passing through a multi-reflecting device with mirrors,^[52] or 2) externally irradiated bodies,^[53] which provide a more homogeneous temperature distribution on the nonirradiated side of the system.

The membrane material properties and the operating conditions (i.e., temperature and oxygen partial pressure) place special demands on the construction materials of the PoC module. Steel parts and sealants must resist operation temperatures between 800 and 900 °C and corrosive conditions under low p_{O_2} sufficiently long such that the performance of the PoC module can be evaluated. As sealant of the ceramic membranes to the metal housing components reinforced glass sealants are excellent candidates.^[54] To adjust the CTE of the glass to the membrane material STF25, adding a metallic filler material such as silver to the glass matrix is a feasible strategy.^[45] This can increase the sealants CTE to avoid a mismatch in thermal expansion between membrane and glass sealant, and glass sealant and steel frame. The steel must closely match the ceramic membrane's CTE. Furthermore, the steel components must be suitable for high-temperature application, oxidation, and corrosion resistant and ideally form protective oxide surface scales to prevent poisoning of the membrane material. Accordingly, high Cr

ferritic steels and alumina-forming steels seem to be the most promising materials for the metallic housing parts.^[55] Details on the choice of joining and construction materials are discussed in Section 3.3.

Cost assessments from high-temperature fuel cell manufacturing show that the design can be a decisive cost factor. For example, the steel components are found to be the most cost-intensive part in the Jülich F-design.^[56] For this reason, the PoC module design is optimized regarding the metal sheet thicknesses and packing density to reduce steel demand. To further decrease manufacturing costs, particular emphasis was laid on identical parts that are technically simple to produce. The PoC module layout and assembly are presented in Section 4.

3.1. Heat Coupling into the Module

The integration of solar thermal power to the PoC module will be demonstrated experimentally at the HFSS located at the DLR facility in Cologne, Germany. The HFSS provides artificially concentrated sunlight and consists of ten elliptical reflectors with xenon short-arc discharge lamps. The HFSS can provide thermal power at the focal plane of about 20 kW.^[57] For this first experimental demonstration and considering the size of the PoC module, the strategy chosen to homogenize the heat flux distribution from the HFSS includes the concept of integrating an external irradiated body.

Figure 2 shows a schematically configuration designed to meet both temperature requirements for the PoC module: 1) operating temperature in the range of 800–900 °C, and 2) temperature gradient over the module body of less than 50 K. The assembly consists of a rectangular-shaped cavity formed by thermal insulated walls (The inner dimensions of the cavity are $220 \times 280 \times 430$ mm; the wall thickness of the parts is 100 mm, and the material selected for the cavity walls is Altraform-KVS) with a 55 mm diameter aperture in the front, which allows concentrated artificial solar light from the HFSS to enter. The main function of the cavity is to reduce thermal losses to the surroundings due to convection and radiation. (The PoC module represented by a rectangular body of dimensions: $120 \times 220 \times 25$ mm) is placed inside the cavity with its largest surface area located in the direction of the incoming light beams. This spatial configuration increases the absorption of

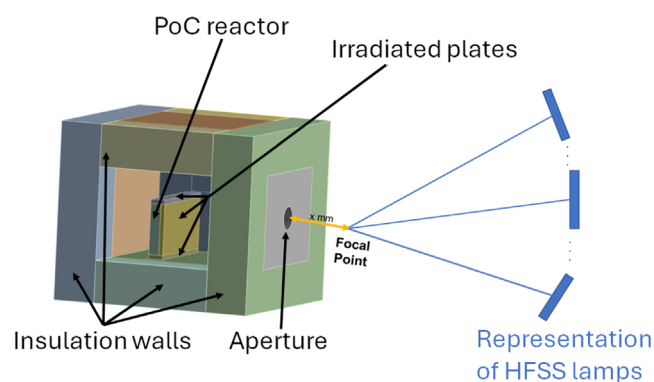


Figure 2. Schematic diagram of the configuration designed to couple the PoC module with the solar thermal power of the HFSS.

thermal energy by the PoC module. A set of three irradiated plates (one at the top, one at the front, and one under the PoC module) has been designed with the main function of reducing the hot spots produced by the peak of the heat flux distribution from the HFSS to the PoC module. To enhance this effect, the thermal conductivity of the irradiated plates material should be as high as possible in the operating temperature range of the PoC module. Copper has a thermal conductivity of 350–370 W mK^{−1} in the temperature range of interest (800–900 °C)^[58] and has been selected as the material for the irradiated plates (The thickness of the irradiated plates is 10 mm to provide good mechanical stability at high temperatures). To control the maximum temperature over the PoC module, the distance between the aperture of the cavity and the FP from the HFSS is varied. In addition, the HFSS has a water-cooled shutter that is used to set the heating rate as well as to adjust the temperature in the system once stable conditions have been reached.

To obtain the temperature distribution of the PoC module, a model was developed implementing the assembly described in the Ansys Academic Research Workbench 2022 R1 software. In this stationary thermal model, the heat flux from the HFSS and the convective losses inside the cavity are introduced as boundary conditions. The flux distribution from the HFSS is obtained using FEMRAY approach and SPRAY software as described in ref. [42], and the convective losses inside the cavity are estimated using the procedure for calculating heat losses inside solar receivers described by Clausen.^[43]

First results have shown that to reach an average temperature in the PoC module of about 850 °C, a distance of 135 mm between the cavity aperture and the FP of the HFSS is required. **Table 1** summarizes the results obtained when using different materials for the irradiated plates. In both cases, the average temperature of the PoC module was about 848 °C. However, some important differences are observed for the maximum temperature and the maximum ΔT in the module. Since copper has a thermal conductivity about 11 times higher than stainless-steel, a better temperature distribution was obtained when the material of the irradiated plates was set to copper. This effect is reflected in the results of the maximum temperature gradient, which corresponded to 71 and 28 K for the stainless-steel and copper cases,

Table 1. Boundary conditions used in the Ansys model to obtain the temperature distribution of the PoC module when different materials for the irradiated plates are used.

Material irradiated plates →		Stainless-steel	Copper
Boundary conditions	Thermal conductivity in T-range (500–900 °C) [W mK ^{−1}]	23–29.3	350
	Total power from HFSS [kW]	3.9	
	Power absorbed inside cavity [kW]	2.5	
	Power reflected (front-side of cavity) [kW]	1.4	
	Convective losses inside cavity [kW]	−483	−487
Temp. results	Max. T in module [°C]	896	864
	Average T in module [°C]	848	848
	Max. ΔT in module [K]	71	28

respectively. As the highest temperature gradient occurred for the stainless-steel plates, spots with a higher temperature are expected for this case (max. T of 896 °C) compared with the copper case (max. T of 864 °C), when the same module average temperature is expected. The selection of copper as the material for the irradiated plates fulfills the module requirement of having a temperature gradient below 50 K.

3.2. Design of PoC Module Process Parameters

The process parameters for the PoC module were calculated using a generalized oxygen transport membranes (OTM) reactor model. Perfect mixing, isothermal conditions, and chemical equilibrium were assumed in the gas compartments. Both reaction chambers are coupled via the Wagner equation to describe the flow of oxygen ions through the membrane. A detailed description can be found in ref. [39].

Due to the underlying assumptions, the modeling approach introduces certain limitations. Neglecting surface exchange kinetics can lead to an overestimation of the oxygen flux, when bulk diffusion is not the rate-determining step in the oxygen transport process.^[59] Additionally, chemical equilibrium modeling tends to underestimate the formation of by-products in the POM reaction, which are primarily CO₂ and H₂O.^[39,60–62] The assumption of perfect mixing can result in an underestimation of the average oxygen flux in longitudinal OTM reactor geometries operated in counter-current flow configuration, as considered in this work, since it neglects the development of concentration profiles in the reactor compartments.^[63]

Despite the limitations of the modeling approach, a validation against experimental data from the literature on frequently studied lab-scale membrane configurations demonstrated that the model reliably predicts the order of magnitude for the oxygen flux and captures the observed trends. Notably, no detailed knowledge of the reaction mechanism is required for this, making the model particularly suitable for preliminary module design.^[39] The code used for the simulations here was published on GitHub.^[40]

Standardized membrane parameters were defined for the simulations as $(\frac{A \cdot \sigma_{amb}}{L})_{stand} \equiv 1$ S, to reduce the number of adjustable parameters, where A is the active membrane area, σ_{amb} is the ambipolar conductivity of the membrane material at application

Table 2. Resulting flow rates and required heat flows for a targeted CH₄ conversion of 95% and a H₂O conversion of 25%.

Parameters and units	Standard membrane parameters	Case I	Case II
Active membrane area [cm ²]	1	167	167
Ambipolar conductivity [S m ^{−1}]	1	2	2
Membrane thickness [μm]	100	350	50
Steam flow rate [mmol min ^{−1}]	0.319	30.4	213
Methane flow rate [mmol min ^{−1}]	0.0803	7.66	53.6
H ₂ production [mmol min ^{−1}]	0.0796	7.6	53.2
Syngas production [mmol min ^{−1}]	0.233	22.2	156
Required heat for reaction [W]	0.287	27.4	192

temperature, and L is the membrane thickness. The temperature was set to 850 °C. Results for the H_2 production on the steam line, H_2O conversion on the methane line, CH_4 conversion on the methane line as well as the CO selectivity of the produced syngas for standardized membrane properties (see Table 2) are shown in Figure 3. These were evaluated as:

$$H_2 \text{ production} = 2j_{O_2} \cdot A \quad (5)$$

$$H_2O \text{ conversion} = \frac{\dot{N}_{H_2O,in} - \dot{N}_{H_2O,out}}{\dot{N}_{H_2O,in}} \quad (6)$$

$$CH_4 \text{ conversion} = \frac{\dot{N}_{CH_4,in} - \dot{N}_{CH_4,out}}{\dot{N}_{CH_4,in}} \quad (7)$$

$$CO \text{ selectivity} = \frac{\dot{N}_{CO,out}}{\dot{N}_{CH_4,in} - \dot{N}_{CH_4,out}} \quad (8)$$

where j_{O_2} is the oxygen flux through the membrane in $\text{mol}/(\text{m}^2 \cdot \text{s})$, $\dot{N}_{i,in}$ is the molar flow rate of species i at the module inlet, and $\dot{N}_{i,out}$ is the molar flow rate of species i at the module outlet.

Although it would be desirable to maximize H_2 production, H_2O and CH_4 conversion, they contradict each as: 1) An increase

in steam flow rate results in an increase of H_2 production and CH_4 conversion but a decrease in H_2O conversion. 2) An increase in methane flow rate results in an increase of H_2 production and H_2O conversion but a decrease in CH_4 conversion. 3) Simultaneously increasing both flow rates, increases the H_2 production but decreases the H_2O and CH_4 conversion. 4) A high CO selectivity (>95%) is achievable in a large operation range.

As a compromise, a H_2O conversion of 25% and a CH_4 conversion of 95% were set as targets for the design. For the standardized membrane parameters, these are achieved for a steam flow rate of $0.319 \text{ mmol min}^{-1}$ and a methane flow rate of $0.0796 \text{ mmol min}^{-1}$. As mentioned above, assuming chemical equilibrium tends to underestimate the by-product formation in the POM reaction, likely to an overestimation of the evaluated CH_4 conversion and CO selectivity. In the experiment, these values will therefore also depend on the catalyst used.

The reactions taking place in the module are net endothermic, which requires a heat flux to prevent membranes from cooling down. This results from the difference between the total enthalpy at the outlet and the inlet of the module. For the calculation, the thermodynamic data were taken from ref. [64].

Table 2 summarizes the obtained results for the defined standardized membrane parameters. These are furthermore scaled proportionally to the parameters expected for the PoC membrane

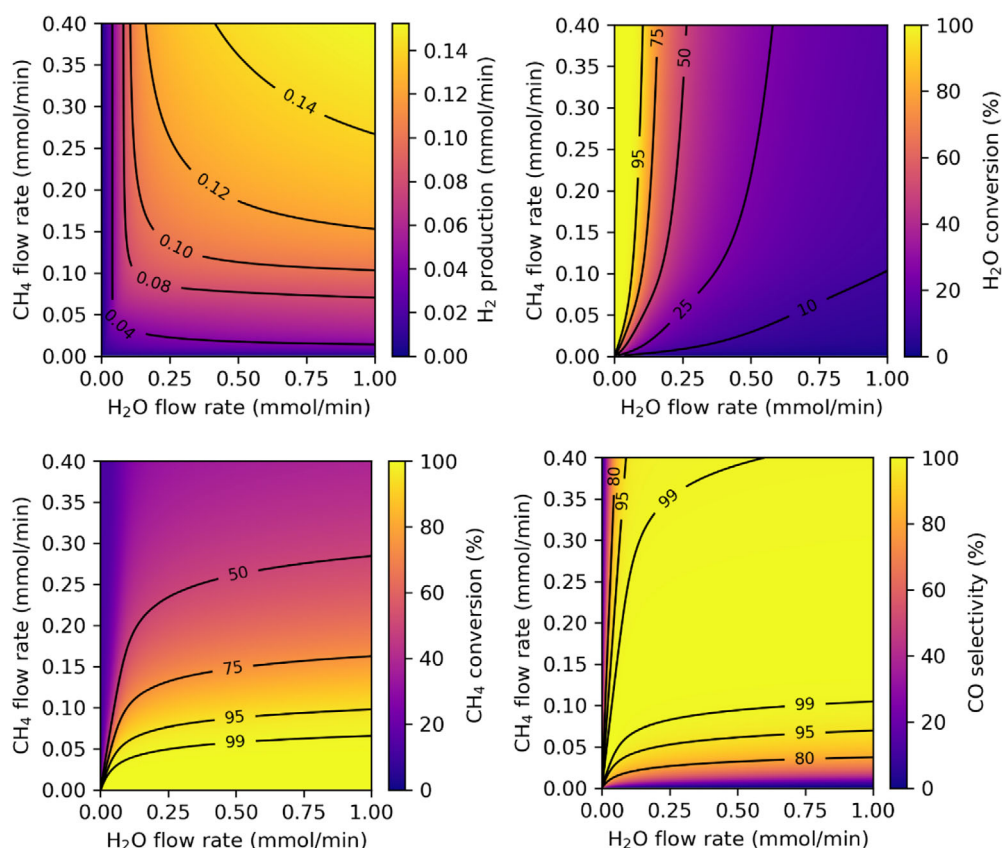


Figure 3. Results of the perfectly mixed reactor model for standardized membrane parameters of 1 cm^2 membrane area, an ambipolar conductivity of 1 S m^{-1} , and a membrane thickness of $100 \mu\text{m}$: the upper left graph shows the H_2 production on the steam line, the upper right graph shows the H_2O conversion on the steam line, the lower left graph shows the CH_4 conversion on the methane line, and the lower right graph shows the CO selectivity on the methane line.

module experiments. A case for planned future prototypes is also estimated here in which significantly thinner supported membranes of 50 μm are assumed (case II in Table 2). The ambipolar conductivity of STF25 at 850 $^{\circ}\text{C}$ was taken from ref. [36]. It should be noted here that the ambipolar conductivity reported in the referenced study was obtained from oxygen permeation experiments using different gases than those considered here. As its dependence on the oxygen partial pressure is unknown, this introduces an uncertainty in the estimation of process parameters.

Due to the limitations of the model described above and the unknown oxygen partial pressure dependence of the ambipolar conductivity, the presented flow rates serve only as a starting point for the experiments. Based on the measured H_2O conversion, it is planned to simultaneously gradually increase or decrease the steam and methane flow rates during the experiments to determine the actual operation point at which 25% H_2O conversion is achieved.

3.3. Material Selection for the PoC Module

The material selection for successful integration of the STF25 membranes into PoC module is based on three interrelated tasks: 1) membrane to membrane window sheet sealant, 2) selection of a thermo-chemically compatible steel for sealant/STF25 and 3) gas-tight joining of the steel components to each other.

The starting point for the selection of materials for structural components and joining material is the CTE of the membrane material. Material in direct contact with the membrane, i.e., sealant for task 1, must remain thermo-chemically compatible with the membrane material. Glass sealants are suitable candidates for high-temperature sealing. A well-investigated and approved system for joining of ceramic to metal is Jülich's glass H based on the BaO-CaO-SiO_2 system long term joining properties demonstrated in SOC applications.^[54,65,66] In this case, the glass ceramic seal was shown to maintain its mechanical integrity for 100 000 h of service. The formation of chromia-enriched barium silicate crystals at the glass-metal-air three-phase interfaces was observed, resulting from the interaction between the glass solder and the volatile chromium species present in the steel.^[66] To date, no interactions between STF25 and glass solder have been observed in short-term applications.^[45] However, given the potential implications for interdiffusion effects, it is imperative that these interactions be thoroughly investigated over extended periods of time. However, glass H, with $9.6 \times 10^{-6} \text{ K}^{-1}$,^[67] has a lower CTE than STF25 with $12\text{--}14 \times 10^{-6} \text{ K}^{-1}$.^[36] To adjust the CTE to ceramic mixed conductors such as STF25, Li et al. developed composite sealant consisting of 60 wt% glass H and 40 wt% silver as filler material, labeled HAg40. HAg40 has a CTE of $12.4 \times 10^{-6} \text{ K}^{-1}$ with good wetting behavior and chemical compatibility to STF25, making it an excellent sealant for the membrane.^[45] As the degree of crystallization of glass-ceramic sealants increases with operating time and temperature, the brittle fracture properties also increase. Insufficient matching of the CTE of the materials to be joined and the glass solder can result in mechanical stresses during temperature changes and joint failure. This can not only cause the joint to lose its sealing properties but also damage the fragile ceramic membrane. Therefore,

thermocycling for the proof-of-concept module should be avoided where possible.

Selection of a thermo-chemically compatible steel for HAg40 composite sealant and STF25 membrane is not only determined by its CTE, but also by oxidation-, and corrosion resistance. Of particular importance is the formation of protective oxide surface scales to prevent the membrane from poisoning. High Cr-containing ferritic and alumina-forming steels were screened. The most promising high Cr ferritic steels with similar expansion behavior to STF25 are Crofer 22 APU (EN 1.4760; UNS S44535), Sicromal 10 (EN 1.4742; AISI 442), and Aluchrom Y Hf (EN 1.4767; UNS K92500) as depicted in **Figure 4**. In general, ceramics should be loaded ideally without stress, or in case stress cannot be avoided, with compressive stresses, as tensile stresses will cause them to fail. To avoid tensile bond stresses in the membrane, the contraction of the membrane during cooling after the joining process must be equal to or less than the contraction of the metallic joining partner. This is not the case for Crofer 22 APU, which rules this material out as a structural component in direct contact with the membrane. Sicromal 10 and Aluchrom Y Hf contract during cooling more than STF25, which leads to compressive stresses in a joined structure. The difference in contraction between Sicromal 10 and STF25 is lower compared to Aluchrom Y Hf, which results in a less compressive load in the membrane. Due to the lower expected compressive stress of the membrane, Sicromal 10 is the preferred structural material in contact with the membrane.

The chemical compatibility between steel and sealant, as well as between sealant and membrane, was analyzed by means of scanning electron microscopy/energy dispersive X-ray spectroscopy investigations on polished cross-sections of the joined samples.

The sealant HAg40 and STF25 showed chemical compatibility and gas tightness. A thin transition layer formed between membrane and HAg40 sealant after the joining process ensures good chemical bonding. Aluchrom Y Hf formed an Al_2O_3 layer at the

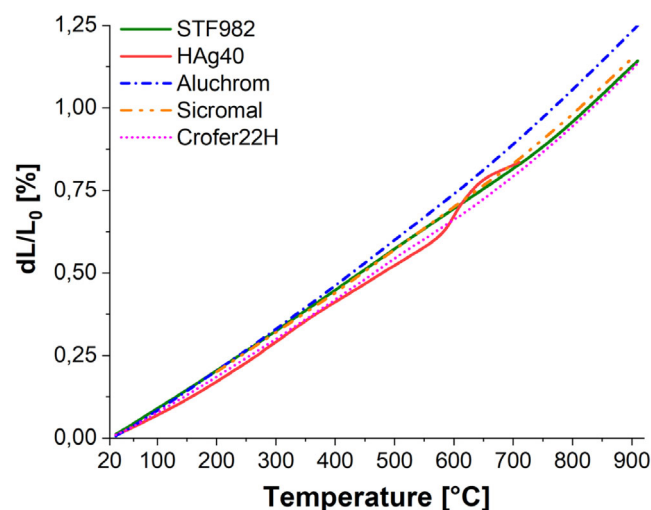


Figure 4. Comparison of the thermal relative length change for specific ferritic steels in comparison to the sealant material HAg40 and the membrane material STF25.

contact surface to HAg40 during joining, which improves the strength of the connection by the formation of chemical bonds with the glass matrix. A detailed analysis can be found in ref. [45].

The joints between STF25 membrane and each of the three steel types were qualified using the pressure drop method on at least three samples. For the combinations, STF25 with Aluchrom Y Hf and STF25 with Sicromal 10, all joined samples showed a leakage rate of $<10^{-6}$ mbar·l·s⁻¹. The samples of the combination of STF25 and Crofer 22 APU failed by fracture of the membrane by tensile stresses while cooling after the joining process. As a result, Crofer 22 APU was excluded as steel material for joining the membrane.

Steel availability in the required sheet thicknesses must be considered as well. Restricted availability of sheets with a thickness of more than 2 mm leads to the exclusion of Aluchrom Y Hf for the manifold frames and the cover and base plates. Therefore, membrane window sheets for direct contact with the membrane can be made of Aluchrom Y Hf or Sicromal10. Cover and base plates and manifold frames could be fabricated of Sicromal10 or Crofer22APU due to the availability. This results in the material combinations Aluchrom Y Hf/Crofer 22 APU, Aluchrom Y Hf/Sicromal10, and Sicromal/Crofer 22 APU.

Sealing tests between these material combinations were performed either using HAg40 or the composite of glass “H” with yttrium-stabilized zirconia fibers as filler (H-F), which is the standard joining material of Jülich SOC.^[54] H-F offers the advantage of being less expensive than composite solder using silver and offers the possibility of using a technology that has already been proven.^[68] Sealing tests were performed according to Section 3. When using H-F sealant, Crofer 22 APU can only be joined with Crofer 22 APU and not with any of the other two steels. Using HAg40, the joining of Crofer 22 APU and Sicromal 10 is possible. Aluchrom Y Hf can be joined against Aluchrom Y Hf with both composite solders. However, the combination of Aluchrom Y Hf and Sicromal 10 is only possible with HAg40. Due to its favorable CTE between Crofer 22 APU and Aluchrom Y Hf, Sicromal 10 is suitable for joining between these two different steels with HAg40 (see Table 3).

These tests are considered sufficient for a proof-of-concept module whose service life is designed for up to 100 h without significant thermocycling in a controlled lab environment. In real applications, material properties such as material embrittlement, mechanical properties at temperatures above 800 °C with

simultaneous hydrogen contact, and corrosion behavior must be investigated in detail to prevent failure of the components outside of safe laboratory conditions.

In conclusion, Crofer 22 APU is not suitable as joining partner for the ceramic membrane made from STF25 in combination with the available glass composite sealants. Aluchrom Y Hf, which is suitable for joining the membrane by means of HAg40, is not available with a thickness of more than 2 mm on market, which rules the material out, for the sake of simplicity. From the mechanical perspective, it is advantageous to use a single type of metal for all layers of the module to avoid risks such as stresses in the sealant and to ensure straightforward production.

All in all, Sicromal 10 fulfills all requirements in terms of joinability in combination with the ceramic membrane and HAg40, availability in all required sheet thicknesses and joinability with the low-cost standard gaskets from SOC. In addition, the price for Sicromal 10 is lower for small batch sizes than for Crofer 22 APU or Aluchrom Y Hf.

3.4. Resulting Functional Specifications for the PoC Module

A precise and thorough definition of the requirements is crucial for the success of the PoC module. Table 4 summarizes the results of the simulations on heat integration and the resulting geometric dimensions as well as in-depth investigations into compatible material combinations. The specifications result from these analyses are shown in Table 4.

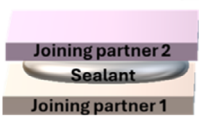
These specifications were translated into the PoC membrane module design based on the Jülich F10-SOC design, which was significantly simplified to reduce material consumption and costs.

4. Design of PoC Membrane Module

The key functions of the membrane module are to accommodate the membranes and create the leak-free gas chambers. Glass-composite sealants hermetically seal the membrane to the metallic housing, avoiding mechanical stresses caused by the differing thermal expansion of the materials. All of this must be achieved over the full temperature range from room temperature up to

Table 3. The joint/seal combinations between the steels using glass–silver (HAg40) or glass–YSZ (H–F) composite sealants. The joints with a leak rate below the threshold of 10^{-7} mbar·l·s⁻¹ are indicated in green, leak rate above the threshold in red, respectively.

Joining partner 1 →	Crofer 22 APU		Aluchrom Y Hf		Sicromal 10		Joining partner 2 ↓
Sealant →	HAg40	H-F	HAg40	H-F	HAg40	H-F	
							Crofer 22 APU
							Aluchrom Y Hf
							Sicromal10



Joining partner 2

Sealant

Joining partner 1

Table 4. Specifications for the PoC membrane module design according to the performed analyses. Left column describes the requirements, the right column describes the proposed solutions.

Materials:	Proposed solutions
Material for housing components with oxidation and corrosion resistance at 850 °C with CTE compatible to membrane material	Sicromal 10 (AN 1.4742, AISI 442)
Sealant for gas tight joining of Membranes to steel	HAg40
Sealant for steel-to-steel joining	H-F
Piping	ferritic heat-resistant chrome steel
Module dimensions:	
Number of membranes per layer	4 membranes of 48 mm diameter and an active diameter of 36.5 mm
Number of layers to achieve in total >160 cm ² open membrane area	4 layers
Manifold height factor to achieve double the throughput for gas compartments with 8 membranes compared to gas compartments with 4 membranes	1.26
Standardized steel parts suitable for mass production	Use of simple geometries
Scalable design	Use of standard repeating units
Pipework:	
Prevent gases from condensation	Sufficient distances between the pipes to install heating jackets and insulation to reduce losses
Temperature measurement of process gases	Access points for thermocouples within the pipework
Easy membrane module change	Swagelok connections in cold zone

850 °C during operation. The module is operated without cross-membrane pressure differences.

Due to the similarities in the requirements, the Jülich F10-SOC design is a good starting point for the membrane module and ensures compatibility with existing tooling and test equipment. Like an SOC stack, the membrane module is built up from individual layers comprising window sheets, manifold frames, cover, and connection plates, as shown in **Figure 5**.

Window sheets (in green) are used to carry four membranes of a diameter of 48 mm each and to seal the gas spaces against each other. The active membrane diameter accessible to the process gases is 36.5 mm each to achieve 167 cm² of open membrane area with four layers. At the front and end of the window sheets, are three gas ports forming the gas inlet (outer holes) and the gas outlet (inner hole).

Manifold frames (brown) create the gas chambers for the process gases and guide their direction of flow, making interconnects as for SOC stacks superfluous. The design doubles the membrane surface area in the center gas compartments compared to the external gas compartments, which enables the utilization of higher process gas flow rates. To achieve double the flow rate in the middle manifold, a height factor of 1.26 was foreseen, assuming a planar flow between two plates. By swapping the orientation of the frame plates in each consecutive layer, the inner or outer holes in the window sheets are sealed off, which directs the process gases to the desired side of the membrane or passes the gas on to the next level. Hereby, methane is directed through the middle and the two outer layers, whereby, steam is directed through the remaining two planes, in which the membranes face each other.

In contrast to the SOC cells, contacting and supporting the membranes is not necessary, but the window sheet must be prevented from sagging at elevated temperatures. For this reason, 10 × 10 mm² square plates are to be joined in the center of each module as well as near the outlet.

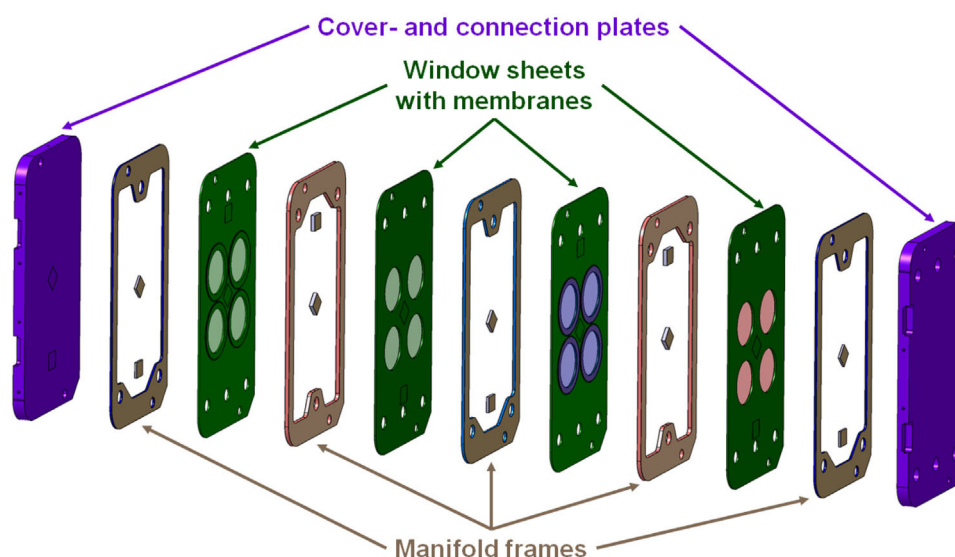


Figure 5. Explosion view of the membrane module comprising of window sheets (green), manifold frames (brown), and cover- and connection plates (purple).

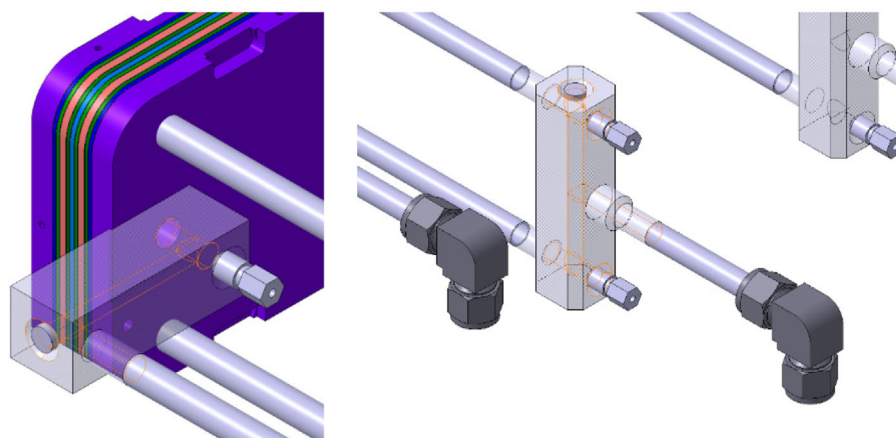


Figure 6. Construction details of the pipework. Left: outrigger, welded to the connection plate. Right: splitter for the feed gases and piping with Swagelok connection to adjacent equipment. Both components with feedthroughs for thermocouples.

Pipes for the feed of steam and methane and the removal of product gases are required and to connect the membrane module to the process components and test equipment. The pipework is constructed to ensure efficient and reliable performance and to minimize potential issues such as leaks and condensation. To realize low leak rates for the overall system over a temperature range from room temperature up to 850 °C, welded pipe connections were designed. Process gases at the inlets are prevented from condensation by using insulation heating cables before entry to the module. Connection points for thermoelements are foreseen to enable the temperature of process gases to be tracked.

There must be adequate space between the welded connections to allow for metal inert gas welding, however, this space is not provided by the envelope dimensions of the membrane module. This was solved by replacing the pipe connections at the outlets of the module with a cross-drilled outrigger which offers sufficient space between the weld seams, as depicted in **Figure 6** (left). This additional part was designed to allow the integration of a thermocouple to measure the outlet temperature of the process gases. This outrigger is connected to the connection plate (purple) with leak-tight welds. Because steam and methane

are fed into the module split across two inlets to give symmetrical gas distribution within the module, a component was needed to split the incoming fluid into two separate streams and to mount thermocouples to track gas temperatures. This splitter is in the modules cold zone and can be seen in **Figure 6** at the right.

The thermal expansion of the module and the piping in the hot zone is compensated in the cold zone by flexible components at lower temperature. The length of the tube was dimensioned to ensure an adequate cooling distance for the gases when utilizing Swagelok fittings. This allows the quick and easy replacement of the PoC module.

An overview of the prototype membrane module including the pipework can be seen in **Figure 7**.

5. Conclusion

The PoC membrane module for solar thermal water splitting was developed with the aid of process simulation and heat integration. The simulation identified optimal flow rates at 850 °C for steam (30–213 mmol min⁻¹) and methane (8–54 mmol min⁻¹), depending on membrane performance. These flow rates were used to size the gas chambers for a membrane area of 167 cm². Key design elements focused on ensuring homogeneous heat distribution and controlling maximum temperatures between 800 and 900 °C during direct irradiation. This was accomplished by adjusting the FP of the HFSS and using irradiated copper plates to mitigate hot spots. The HFSS's water-cooled shutter was employed to control the heating rate and to stabilize the temperature once optimal conditions were reached. The simulations presented in this article provide initial indications of general trends and identify interesting operating parameter ranges for the design of a PoC module. However, to proceed with the simulation-based design choices for approaching optimum operating ranges, to compare membrane processes, and to compare the membrane-assisted water splitting with state-of-the-art solar thermal processes, further research is necessary on the material (i.e., ionic and electronic conductivity under relevant atmospheres), oxygen transport (i.e., understanding the surface reactions), and the process (i.e., formation of byproducts).

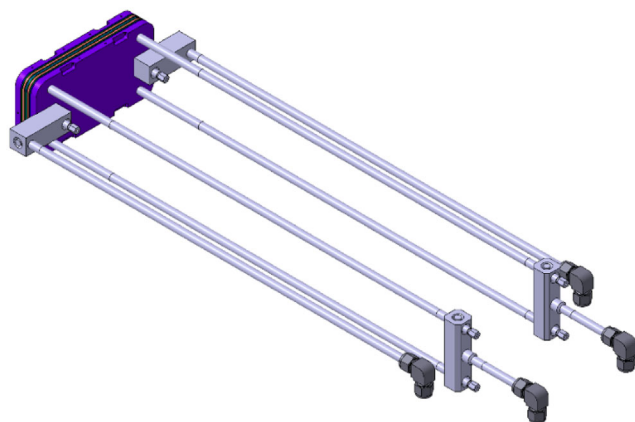


Figure 7. Overview of the PoC membrane module.

The material concept was tailored to the membrane material properties, preventing thermal stresses and ensuring gas-tight sealing of the membranes at an operating temperature of 850 °C under reducing and corrosive conditions. A glass-silver composite sealant was selected for membrane-to-steel joining due to its excellent chemical compatibility and matching thermal expansion properties. For the large-area joining between the steel layers, a glass-YSZ composite sealant was used because of its low cost and appropriate thermal expansion properties. Sicromal 10 steel was chosen for the module's construction due to its corrosion resistance, suitable thermal expansion behavior in comparison to the membrane and glass-composite sealants, as well as its availability and cost-effectiveness. However, there is a lack of data regarding the long-term stability of the components in the relevant atmospheres and temperatures. This is a crucial aspect that must be addressed in future research.

The PoC module features a stack design with parallel-oriented, membrane-containing layers. Manifold frames form the gas chambers for the process gases and direct their flow. Welded pipe-work was designed to supply steam and methane and remove product gases, while minimizing condensation and leakage.

According to simulation, this membrane module can produce 7–51 mmol min⁻¹ of hydrogen and 22–156 mmol min⁻¹ of syn-gas, with conversion rates of 25% and 95%, respectively, at 850 °C with 167 cm² membrane area.

Acknowledgements

The authors are grateful for the financial support received from the German Federal Ministry of Education and Research within the MESOWAS project (grant no. 03SF0648). The authors would also like to thank A. Cramer, D. Federmann, T. Beyel for their technical support, T. Koppitz for dilatometric measurements, and S. Brendelberger, Y. Kadohiro, and C. Willsch for fruitful discussion on strategies to homogenize the temperature distribution.

Conflict of Interest

The authors declare no conflict of interest.

Data Availability Statement

The data that support the findings of this study are available on request from the corresponding author. The data are not publicly available due to privacy or ethical restrictions.

Keywords

membrane reactors, module design, oxygen transport membranes, solar thermochemical hydrogen production, water splitting

Received: November 19, 2024

Revised: March 28, 2025

Published online:

- [1] S. Singh, S. Jain, P. S. Venkateswaran, A. K. Tiwari, M. R. Nouni, J. K. Pandey, S. Goel, *Renewable Sustainable Energy Rev.* **2015**, 51, 623.
- [2] A. Kovač, M. Paranos, D. Marciuš, *Int. J. Hydrogen Energy* **2021**, 46, 10016.

- [3] A. Otto, M. Robinius, T. Grube, S. Schiebahn, A. Praktikno, D. Stollen, *Energies* **2017**, 10, 451.
- [4] V. Vogl, M. Åhman, L. J. Nilsson, *J. Clean. Prod.* **2018**, 203, 736.
- [5] P. J. Megía, A. J. Vizcaíno, J. A. Calles, A. Carrero, *Energy Fuels* **2021**, 35, 16403.
- [6] K. J. Warren, A. W. Weimer, *Sol. Compass.* **2022**, 1, 100010.
- [7] A. Kogan, *Int. J. Hydrogen Energy* **1998**, 23, 89.
- [8] X. Li, Y. Shen, L. Wei, C. He, A. A. Lapkin, W. Lipiński, Y. Dai, C. H. Wang, *Appl. Energy* **2020**, 261, 114229.
- [9] M. E. Ivanova, R. Peters, M. Müller, S. Haas, M. F. Seidler, G. Mutschke, K. Eckert, P. Röse, S. Calnan, R. Bagacki, R. Schlattmann, C. Grosselindemann, L. Schäfer, N. H. Menzler, A. Weber, R. van de Krol, F. Liang, F. F. Abdi, S. Brendelberger, N. Neumann, J. Grobbel, M. Roeb, C. Sattler, I. Duran, B. Dietrich, M. E. C. Hofberger, L. Stoppel, N. Uhlenbruck, T. Wetzels, D. Rauner, et al., *Angew. Chem., Int. Ed.* **2023**, 62, e202218850.
- [10] M. S. Hossain, M. N. Islam, K. Shahriar, M. Muftaba Hasan, M. S. Hossain, *Energy Convers. Manag.* **2025**, 25, 100876.
- [11] Y. Mao, Y. Gao, W. Dong, H. Wu, Z. Song, X. Zhao, J. Sun, W. Wang, *Appl. Energy* **2020**, 267, 114860.
- [12] V. Madadi Avargani, S. Zendejboudi, *Energy Convers. Manag.* **2023**, 276, 116539.
- [13] J. R. Scheffe, A. Steinfeld, *Mater. Today* **2014**, 17, 341.
- [14] S. E. Hosseini, M. A. Wahid, *Renewable Sustainable Energy Rev.* **2016**, 57, 850.
- [15] J. E. Funk, R. M. Reinstrom, *Ind. Eng. Chem. Proc. Des. Dev.* **1966**, 5, 336.
- [16] X. Y. Wu, L. Chang, M. Uddi, P. Kirchen, A. F. Ghoniem, *Phys. Chem. Chem. Phys.* **2015**, 17, 10093.
- [17] H. Bouwmeester, P. Gellings, *Handbook of Solid State Electrochemistry*, CRC Press, Boca Raton, FL, United States **1997**, <https://doi.org/10.1201/9781420049305>
- [18] G. Chen, A. Feldhoff, A. Weidenkaff, C. Li, S. Liu, X. Zhu, J. Sunarso, K. Huang, X. Wu, A. F. Ghoniem, W. Yang, J. Xue, H. Wang, Z. Shao, J. H. Duffy, K. S. Brinkman, X. Tan, Y. Zhang, H. Jiang, R. Costa, K. A. Friedrich, R. Kriegel, *Adv. Funct. Mater.* **2022**, 32, 2105702.
- [19] A. S. Ghanem, F. Liang, M. Liu, H. Jiang, A. Toghan, *Chem. Eng. J.* **2023**, 474, 145263.
- [20] M. Lubkoll, M. Ebert, L. Amsbeck, A. Hirt, C. Frantz, J. Rheinländer, R. Buck, *AIP Conf. Proc.* **2022**, 2445, 110005.
- [21] R. Buck, S. Giuliano, *AIP Conf. Proc.* **2019**, 2126, 030010.
- [22] C. Frantz, R. Buck, L. Amsbeck, *J. Energy Resour. Technol.* **2022**, 144, 092107.
- [23] M. Lin, S. Haussener, *Sol. Energy* **2017**, 155, 1389.
- [24] X. Y. Wu, A. F. Ghoniem, M. Uddi, *AIChE J.* **2016**, 62, 4427.
- [25] W. Deibert, M. E. Ivanova, S. Baumann, O. Guillon, W. A. Meulenber, *J. Memb. Sci.* **2017**, 543, 79.
- [26] S. Zhang, T. Li, B. Wang, Z. Zhou, X. Meng, N. Yang, X. Zhu, S. Liu, *J. Memb. Sci.* **2022**, 659, 120772.
- [27] B. Wang, T. Li, Z. Wang, M. H. D. Othman, S. Liu, R. Xiao, *Green Chem.* **2023**, 25, 6930.
- [28] L. L. Anderson, P. A. Armstrong, R. R. Broekhuis, M. F. Carolan, J. Chen, M. D. Hutcheon, C. A. Lewinsohn, C. F. Miller, J. M. Repasky, D. M. Taylor, C. M. Woods, *Solid State Ion.* **2016**, 288, 331.
- [29] N. Nauels, S. Herzog, M. Modigell, C. Broeckmann, *J. Memb. Sci.* **2019**, 574, 252.
- [30] M. Schulz, U. Pippardt, L. Kiesel, K. Ritter, R. Kriegel, *AIChE J.* **2012**, 58, 3195.
- [31] F. Schulze-Küppers, F. Drago, L. Ferravante, S. Herzog, S. Baumann, P. Pinacci, W. A. Meulenber, *Sep. Purif. Technol.* **2019**, 220, 89.
- [32] T. Li, T. Kamhangdatepon, B. Wang, U. W. Hartley, K. Li, *J. Memb. Sci.* **2019**, 578, 203.

- [33] G. He, Y. Ling, H. Jiang, A. Toghan, *ACS Sustain. Chem. Eng.* **2021**, 9, 11147.
- [34] Z. Cao, H. Jiang, H. Luo, S. Baumann, W. A. Meulenber, H. Voss, J. Caro, *Catal. Today* **2012**, 193, 2.
- [35] Y. Liu, V. Motalov, S. Baumann, D. Sergeev, M. Müller, Y. J. Sohn, O. Guillon, *J. Eur. Ceram. Soc.* **2019**, 39, 4874.
- [36] F. Schulze-Küppers, S. F. P. ten Donkelaar, S. Baumann, P. Prigorodov, Y. J. Sohn, H. J. M. Bouwmeester, W. A. Meulenber, O. Guillon, *Sep. Purif. Technol.* **2015**, 147, 414.
- [37] R. Oliveira Silva, J. Malzbender, F. Schulze-Küppers, S. Baumann, O. Guillon, *J. Eur. Ceram. Soc.* **2017**, 37, 2629.
- [38] R. Oliveira Silva, J. Malzbender, F. Schulze-Küppers, S. Baumann, M. Krüger, O. Guillon, *J. Eur. Ceram. Soc.* **2018**, 38, 5067.
- [39] K. Bittner, N. Margaritis, F. Schulze-Küppers, J. Wolters, G. Natour, *J. Memb. Sci.* **2023**, 685, 121955.
- [40] K. Bittner, N. Margaritis, F. Schulze-Küppers, J. Wolters, G. Natour, *Ideal Equilibrium Oxygen Membrane Reactor*, Zenodo, Geneva, Switzerland **2023**, <https://doi.org/10.5281/zenodo.10406046>.
- [41] D. G. Goodwin, H. K. Moffat, I. Schoegl, R. L. Speth, B. W. Weber, *Cantera: An Object-Oriented Software Toolkit for Chemical Kinetics, Thermodynamics, and Transport Processes*, Zenodo, Geneva, Switzerland **2022**, <https://doi.org/10.5281/zenodo.6387882>.
- [42] Y. Kadohiro, V. K. Thanda, B. Lachmann, K. Risthaus, N. Monnerie, M. Roeb, C. Sattler, *Energy Convers. Manag.* **2023**, 18, 100366.
- [43] A. M. Clausen, *J. Sol. Energy Eng.* **1983**, 105, 29.
- [44] F. Schulze-Küppers, S. Baumann, W. A. Meulenber, H. J. M. Bouwmeester, *J. Memb. Sci.* **2020**, 596, 117704.
- [45] X. Li, S. M. Groß-Barsnick, T. Koppitz, S. Baumann, W. A. Meulenber, G. Natour, *J. Eur. Ceram. Soc.* **2022**, 42, 2879.
- [46] N. Sammes, A. Smirnova, O. Vasylyev, *Fuel Cell Technologies: State and Perspectives*, Springer-Verlag, Berlin/Heidelberg **2005**, <https://doi.org/10.1007/1-4020-3498-9>.
- [47] L. Blum, L. G. J. de Haart, J. Malzbender, N. Margaritis, N. H. Menzler, *Energy Technol.* **2016**, 4, 939.
- [48] F. Thaler, Q. Fang, U. de Haart, L. G. J. Bert De Haart, R. Peters, L. Blum, *ECS Trans.* **2021**, 103, 363.
- [49] M. K. Nikoo, N. A. S. Amin, *Fuel Process. Technol.* **2011**, 92, 678.
- [50] D. Pashchenko, I. Makarov, *Energy* **2021**, 222, 119993.
- [51] G. Ambrosetti, P. Good, *Sol. Energy* **2019**, 183, 521.
- [52] J. C. G. Pereira, K. Rahmani, L. G. Rosa, *Energies* **2021**, 14, 1828.
- [53] M. Tou, R. Michalsky, A. Steinfeld, *Joule* **2017**, 1, 146.
- [54] S. M. Gross, D. Federmann, J. Remmel, M. Pap, *J. Power Sources* **2011**, 196, 7338.
- [55] W. J. Quadackers, J. Piron-Abellan, V. Shemet, L. Singheiser, *Mater. High Temp.* **2003**, 20, 115.
- [56] S. Harboe, A. Schreiber, N. Margaritis, L. Blum, O. Guillon, N. H. Menzler, *Int. J. Hydrogen Energy* **2020**, 45, 8015.
- [57] G. Dibowski, A. Neumann, P. Rietbrock, C. Willsch, J.-P. Säck, K.-H. Funken, Der neue Hochleistungsstrahler des DLR - Grundlagen, Technik, Anwendung, 10. Kölner Sonnenkolloquium, **2007**. <https://elib.dlr.de/68533/>.
- [58] R. P. Minneci, E. A. Lass, J. R. Bunn, H. Choo, C. J. Rawn, *Int. Mater. Rev.* **2021**, 66, 394.
- [59] H. J. M. Bouwmeester, H. Kruidhof, A. J. Burggraaf, *Solid State Ion.* **1994**, 72, 185.
- [60] X. Li, J. Grace, A. Watkinson, C. Lim, A. Ergüdenler, *Fuel* **2001**, 80, 195.
- [61] A. C. D. Freitas, R. Guirardello, *Int. J. Hydrogen Energy* **2014**, 39, 17969.
- [62] A. Gambarotta, M. Morini, A. Zubani, *Appl. Energy* **2018**, 227, 119.
- [63] K. Bittner, N. Margaritis, F. Schulze-Küppers, J. Wolters, G. Natour, *Membranes* **2024**, 14, 219.
- [64] G. P. Smith, D. M. Golden, M. Frenklach, N. W. Moriarty, B. Eiteneer, M. Goldenberg, C. T. Bowman, R. K. Hanson, S. Song, W. C. J. Gardiner, V. V. Lissianski, Z. Qin, GRI-Mech 3.0, n.d. http://www.me.berkeley.edu/gri_mech/.
- [65] L. Blum, Q. Fang, S. M. Groß-Barsnick, L. G. J. Bert de Haart, J. Malzbender, N. H. Menzler, W. J. Quadackers, *Int. J. Hydrogen Energy* **2020**, 45, 8955.
- [66] N. Menzler, D. Sebold, S. Zischke, J. Zurek, D. Naumenko, S. Gross-Barsnick, *ECS Trans.* **2021**, 103, 1047.
- [67] S. M. Gross, T. Koppitz, J. Remmel, J. B. Bouche, U. Reisgen, *Fuel Cells Bull.* **2006**, 2006, 12.
- [68] D. Federmann, H.-R. Zerfass, S.-M. Groß-Barsnick, Method for producing a solder glass green seal **2019**. <https://patents.google.com/patent/US10170775B2/en>.